Exploration of metal-layered double hydroxide composite material for hybrid capacitor produced by facile and efficient electrodeposition process

Gift Rutavi, Delvina Japhet Tarimo, Vusani Muswa Maphiri, Vianney Ngoyi Kitenge and Ncholu Manyala*

Department of Physics, Institute of Applied Materials, SARChI in Carbon Technology and Materials, University of Pretoria 0028, South Africa
*Corresponding author's email: ncholu.manyala@up.ac.za, Tel.: + (27)12 420 3549.

Abstract

Manganese cobaltite (MCO) with an empirical formula $Mn_{2-x}Co_{1+x}O_4$ and cobalt-nickel layered double hydroxide (CN-LDH) composite were synthesized through a dual-step electrodeposition approach. This process commenced with cyclic voltammetry (CV) electrodeposition of manganese cobaltite (MCO) on nickel foam (NF) followed by annealing in air. The next step was the CV electrodeposition of CN-LDH on MCO. The enhanced composite material MCO-2.5@CN-LDH yielded a remarkable specific capacity of 415.9 mAh g^{-1} at a specific current of 1 A g^{-1} in a three-electrode configuration using 2 M KOH electrolyte. The electrodeposition method is credited for producing these competitive results, since the method excludes polymeric binders which would make it necessary to include conductive additives to compensate for the increased resistivity in the electrode materials. This positive electrode and the activated carbon from cooked chicken bone waste (CCBW) as the negative electrode were assembled into hybrid supercapacitor device (MCO-2.5@CN-LDH//CCBW) using the same electrolyte. The device generated a specific energy of 55.8 Wh kg^{-1} corresponding to a specific power of 940.4 W kg^{-1} at 1 A g^{-1}. A device stability measurement at 10,000 galvanostatic charge-discharges (GCD) at 7 A g^{-1} produced a capacity retention of 81.6 % and coulombic efficiency of 99.8 %. Owing to these promising

results, the fabricated materials proved to be capable to be employed as high specific energy supercapacitor.

Keywords: Layered double hydroxide; Energy storage; Spinels; Specific capacity; Hybrid capacitor.

1.0 Introduction

The use of non-renewable resources is always exerting a lot of pressure on the enviroment. Looking at the tremendous rate of the destruction, the shift from non-renewable to renewable sources of energy that are more environmentally friendly is long overdue. The intermittent nature of renewable energy sources is hindering this transfer and this is worsened by their availability in inadequate quantities [1–4].

These challenges can be alleviated by focusing resources on sourcing, examining, and improving storage devices for renewable energy. Among existing energy storage devices, supercapacitors have generated a lot of interest. They are endowed with some beneficial attributes compared to their counterparts such as batteries and fuel cells. These include long cycle life, greater specific power, and quicker charge-discharge. Above all these, they are more environmentally friendly compared to other storage devices. [5–8].

There are at least three classes of supercapacitors, the most common are electric double-layer capacitors (EDLC), pseudocapacitors (PC), and battery-type capacitors (BT). EDLC electrode materials, which store energy through charge separation at the electrolyte-electrode interface profit from possessing very large specific surface areas (SSA), wide operating potential windows and great electrical conductivities. These properties lead to huge specific power and faster charge discharge. PC and BT benefit from high theoretical

specific capacities and specific energies due to rapid redox reactions at their electrolyte/electrode interface [9–11].

Layered double hydroxide (LDH) nanocomposites are promising functional materials because they incorporate the properties and features of the polymer and inorganic phases. The intercalation with functional nanomaterials possesses desirable electronic, magnetic, optical and piezoelectric properties for various universal applications such as medicine, functional coatings, microelectronics, energy storage and harvesting. CN-LDH is an essential bimetallic compound which has generated a lot of interest in energy storage research due to high specific capacity which is attributed to an abundant reactions sites and unique layered structure [12–15]. However, the two-dimensional structure of CN-LDH leads to aggregation of materials and severe reduction in electrical conductivity leading to a rise in electric resistance during the GCD processes [16–18]. It is recommended to assemble composite electrodes by complementing LDHs with materials with much better electrical conductivities.

Metal cobaltites have been thoroughly investigated for use in supercapacitors as positive electrode because they possess some advantageous features which include very high electrical conductivity and reversibility. With a very large theoretical specific capacitance of 3620 F g^{-1}, MCO is a suitable candidate for synthesizing a high performance composite electrode with CN-LDH. This is because the manganese (Mn) ions enhance the electrical conductivity. The Mn^{3+} also benefit from the Jahn-Teller effect which improves ions diffusion and avails more reversible phase transformation [19]. The cobalt (Co) ions increase the electrochemical activity of the composite [20]. However, low cyclic stability limit their practical application. This can be alleviated through synthesis of a hybrid electrode consisting of a metal cobaltite and an LDH. For instance, Wang et al. hydrothermally

synthesized glass-like $NiCo_2O_4$@NiCo-LDH on a carbon cloth which yielded a phenomenal areal capacitance of 5810 mF cm^{-2} at a surface current density of 1 mA cm^{-2} [21].

Synthesis methods also play a very crucial role in the performance of electrode. Binder-free synthesis approaches are favoured because binders which are usually polymeric materials introduce significant resistance to to the electrode materials. To compensate for this, conductive additives have to be added to the electrode materials. Electrodeposition is a very important binder-free synthesis method as it possesses many advantages over other binder-free approaches such as the the successive ionic layer adsorption and reaction (SILAR) methods. These advantages include a very strong adhession between the active material (AM) and the current collector. This method is also very simple, efficient, cost effective and it provides a facile way of controlling the thickness of the films by varying parameters such as electrodeposition duration time, scan rate and number of electrodeposition cycles. There is a great electron transfer between the substrate and the material since the materials is grown directly on the substrate [22–25].

In this study we report the synthesis MCO-2.5, CN-LDH, and MCO-2.5@CN-LDH as positive electrodes (positrodes) through the process of electrodeposition. The composite electrode: MCO-2.5@CN-LDH displayed the best electrochemical performances with a specific capacity of 415.9 mAh g^{-1} in 2 M KOH at a specific current of 1 A g^{-1} in a half cell set-up. The electrode further displayed a superb electrochemical stability with a coulombic efficiency of 99.8 % after 5,000 GCD at 7 A g^{-1}. Due to this amazing performance, the composite electrode was incorporated as the positive electrode for hybrid supercapacitor device (MCO-2.5@CN-LDH//CCBW), where CCBW served as the negative electrode. The device yielded a huge specific energy of 55.8 Wh kg^{-1} corresponding to a specific power of 940.4 W kg^{-1}. The hybrid device also showed great stability by producing a capacity retention of 81.6 % and coulombic efficiency of 99.8 % after 10,000 cycles at a gravimetric

current of 1 A g^{-1}. Due to these promising results, the fabricated material has a potential for use as high performance renewable energy storage devices.

2.0 Experimental section

2.1 Materials

All the chemicals were used without further refining. The following chemicals and materials were used in this study: Deionised water (DW), which was extracted using a DRAWELL water purification device. Nickel foam [NF] was bought from Alantum (Munich, Germany). Ethanol [$CH_3 CH_2OH$], Acetone [$(CH_3)_2$ CO], and hydrochloric acid [HCl] were acquired from (Sigma Aldrich, Steinheim, Germany). Nickel nitrate hexahydrate [Ni $(NO_3)_2$•$6H_2O$], manganese acetate hexahydrate [$Mn(CH_3COO)_2$•$4H_2O$], cobalt nitrate hexahydrate [$Co(NO_3)_2$•$6H_2O$], sodium sulphate [Na_2SO_4], sulphur, and sodium sulphide [Na_2S] were all purchased from Merck (Johannesburg, South Africa).

2.2 Preparation of NF substrates

The preparation of NF was done as reported in our previous work [26]. Briefly, NF was shaped into (1 cm × 2 cm) rectangular pieces. The pieces were comprehensively cured by first dipping in 3 M HCl, acetone, followed by absolute ethanol (purity > 99 %), and lastly in DW, each for 20 minutes. These pieces were dried for 12 hours in an oven at 60^o C. The purpose of this rigorous cleansing process was to eliminate the inert hydroxide and oxide layers which form on NF under humid conditions.

2.3 Preparation of MCO on NF electrode

Mn $(CH_3COOH)_2.H_2O$ (0.006 mol) and $Co(NO_3)_2.6H_2O$ (0.012 mol) were mixed in 250 ml DW and stirred for 1 hour to make a homogeneous solution. Na_2SO_4 (0.01 mol) was added to the solution to serve as a morphology directing agent and to prevent the agglomeration of particles. This solution was labelled S1. The electrodeposition was carried out using BioLogic VMP-300 workstation (Knoxville, TN,37,930 USA) operating on the EC-lab V11-30 software (Edmonton, AB, Canada) at room temperature. NF, platinum rod, and Ag/AgCl served as the working electrode (WE), counter electrode (CE), and reference electrode (RE), respectively in a 3-electrode set-up. The electrodeposition was carried out using cyclic voltammetry (CV) at 1.25 mV s^{-1} for 6 cycles in a potential range of -1.2 to 0.5 V vs Ag/AgCl. The electrode which consisted of Co and Mn mixed oxides was then washed in DW and dried at 80^o C in an oven for 5 hours then annealed in air at 200^o C for 1 hour. The purpose of annealing was to transform the phase structure from LDH to the spinel phase [27]. The procedure was repeated at scan rates of 2.5 and 5 mV s^{-1}. The samples were labelled as MCO-1.25, MCO-2.5 and MCO-5 according to the scan rates used for synthesis. The mass loading of the deposited materials on NF were 1.4, 1.1 and 0.8 mg for MCO-1.25, MCO-2.5 and MCO-5 respectively.

2.4 Synthesis of CN-LDH, MCO@CN-LDH and CCBW

The synthesis of CN-LDH was similar to the one reported in our previous work [28]. In brief, 0.01 M each of Ni $(NO_3)_2$•$6H_2O$ and Co $(NO_3)_2$•$6H_2O$ were dissolved in 50 ml of DW and stirred vigorously for 30 minutes to form the homogeneous solution labeled S2. The electrodeposition procedure was identical to that in section 2.3 except that the abovementioned solution (S2) served as the electrolyte. The electrode was labelled as CN-

LDH. The procedure was then repeated, this time with MCO-2.5 as the working electrode, this composite electrode was labelled as MCO-2.5@CN-LDH. CCBW which was used as the negative electrode was produced as detailed in our previous work [29]. The synthesis procedures are illustrated in the schematic in Fig.1.

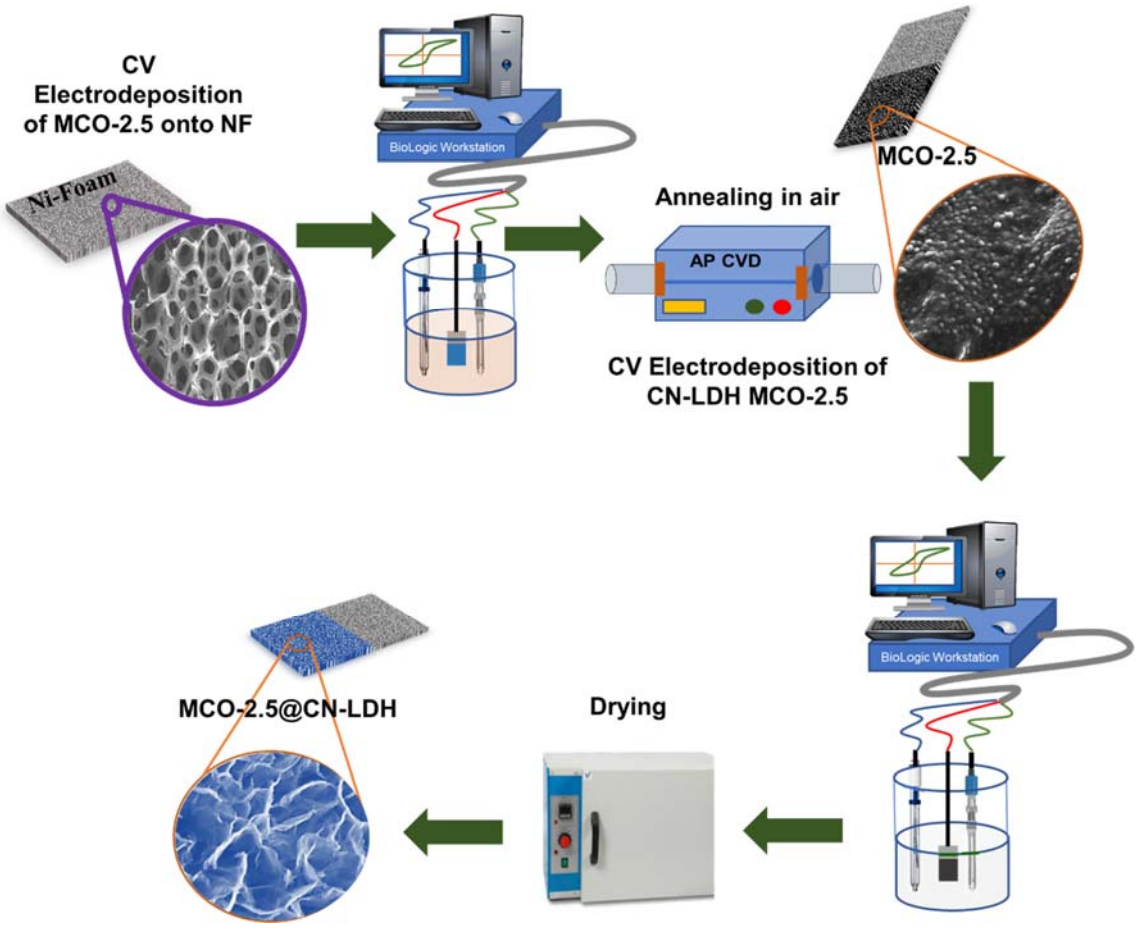

Fig. 1: Schematic illustration of the synthesis of MCO-2.5@CN-LDH electrode.

2.5 Material characterization

The Zeiss Ultra PLUS FEG-SEM (Ashikima Shi, Japan) which operated at 2.0 kV and incorporating the Oxford energy dissipation spectroscopy X-ray (EDS) was used to evaluate the morphology, electrode thickness and elemental composition of MCO, CN-LDH and MCO-2.5@CN-LDH materials. Transmission electron microscopy (TEM) images were obtained from the JEOL JEM 2100-F which operated at 1.0 kV. The X-Ray Diffraction (XRD) was used to analyse the structure of the samples. This makes use of a diffractometer (Brucker 2D PAN analytical BV, Amsterdam, Netherlands), which incorporates Cu $K_{\alpha 1}$ (λ = 0.154061 nm) at 2θ range from 5- 90^{o}. Raman spectroscopy measurements were performed using a WITec alpha-300 RAS+ Confocal micro-Raman microscope (Focus Innovations, Ulm Germany) with a 532 nm laser, spectral acquisition of 300s using a 20X objective with a laser power of 4.5 mW.

2.6 Electrochemical characterization

To evaluate the electrochemical performance of the samples, the Bio-Logic workstation potentiostat was used. In three-electrode arrangement, the CE and RE were similar to those reported in section 2.3. The WE were CN-LDH, MCO and MCO-2.5@CN-LDH. CV, GCD and electrochemical impedance spectroscopy (EIS) were carried out in 2 M KOH for both 3-electrode and 2-electrode set-up (for hybrid supercapacitor device), respectively.

3.0 Results and analysis

3.1 Microstructural characterization and analysis

Fig. 2 displays high magnification SEM micrograms of MCO-1.25, MCO-2.5, and MCO-5. The morphology in Fig. 2(a) shows a mixture of fine and granular nanospheres for the MCO-1.25 sample. The morphology in Fig. 2(b) shows an increase in coarseness in MCO-2.5, revealing a nanosphere morphology with diameters close to 100 nm. This surface structure is endowed with channels which may facilitate ion transport. The nanospheres in Fig. 2(c) belong to MCO-5, these are also coarse but fused together thereby reducing pathways available for ion transport. Fig. 2 (d)-(i) reveals low- and high-resolution SEM images of the synthesized MCO-2.5 CN-LDH, and MCO-2.5@CN-LDH samples, respectively. Fig. 2(d, e) displays nanoflakes morphology of CN-LDH with widths of around 300 nm vertically grown on NF. Fig. 2 (f, g) presents the granular MCO-2.5 nanospheres. Fig. 2(h, i) reveal thin sheets of CN-LDH completely covering the MCO-2.5 nanospheres. Fig S1(a) displays the SEM cross section of MCO-2.5@CN-LDH, where the MCO-2.5 film which has an average thickness of 12 μm is sandwiched by a 8 μm thick CN-LDH film and the NF substrate. Fig S1(b) shows the HRTEM image of MCO-2.5@CN-LDH composite sample. The morphology reveals a cloud of CN-LDH nanoflakes wrapped around the dense MCO-2.5 microstructure. This structure avails more surface area on the electrode essential for ion penetration leading to an increase in redox reactions which contributes to high specific capacity.

Fig. S2 (a)-(d) display the EDS mapping of the MCO-2.5@CN-LDH composite sample. The maps show the composition of oxygen, manganese, cobalt and nickel, respectively within the material. The uniform distribution of O (21.41 %), Mn (1.81 %), Co (38.33 %) and Ni

(38.45 %) elements were observed. The percentage composition of these elements are shown in Fig. S2(e).

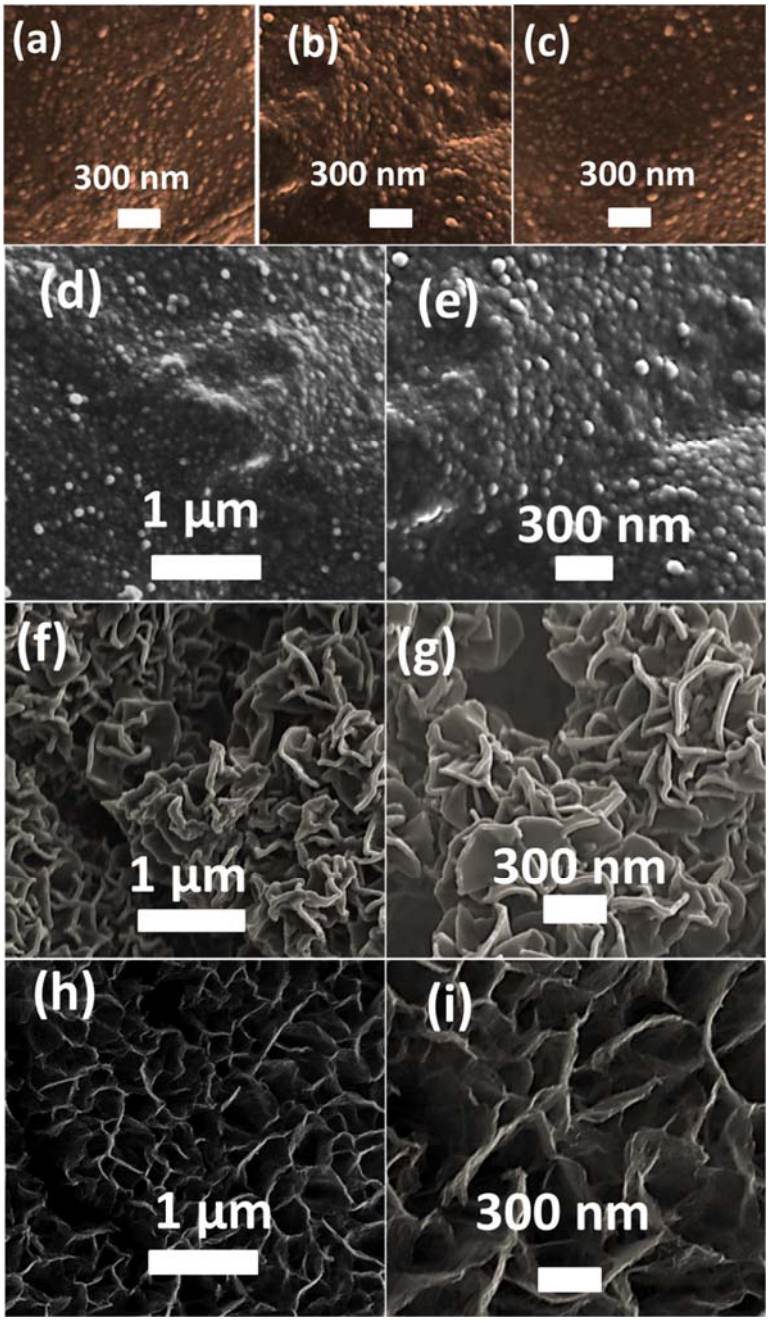

Fig. 2: High resolution SEM micrographs of MCO samples: (a) MCO-1.25, (b) MCO-2.5, and (c) MCO-5, (d, e), (f, g) and (h, i) present low- and high-resolution micrographs of MCO-2.5 CN-LDH, and MCO-2.5@CN-LDH, respectively.

Fig. 3(a) displays the Raman spectrum of MCO-1.25, MCO-2.5 and MCO-5. The A_{1g} and E_g peaks corresponds to Raman shifts at 685 and 492 cm^{-1}, respectively revealing the octahedral nature of the cobaltite. The F_{2g} peak at 512 cm^{-1} is due to the tetrahedral nature of manganese cobaltite. Both phases are present in MCO-2.5 [30]. There is no significant difference in peak intensity implying that the scan rate range of 1.25 to 5 mV s^{-1} is sufficient for the formation of the manganese cobaltite phase in a potential range of -1.2 to 0.5 V vs Ag/AgCl. However, the MCO-2.5 sample appears to have a slightly higher intensity compared to the rest. Fig 3 (b) shows the Raman spectrum of MCO-2.5 CN-LDH, and MCO-2.5@CN-LDH samples. In CN-LDH shows the E_{1g} at 479 cm^{-1} which reveals the presence of O-Ni-O and O-Co-O while F_{2g} and A_{1g} at 546 and 673 cm^{-1}, respectively reveal the presence of Ni-OH and Co-OH bonds [31]. The presence of E_{1g}, F_{2g} and A_{1g} peaks in MCO-2.5@CN-LDH is evidence of the successful combination of the LDH and the spinel.

Fig 3(c) indicates the XRD of MCO-2.5 CN-LDH, and MCO-2.5@CN-LDH samples. The planes correspond to (003), (006), (009), (015), (018), (110) and (113) occur at diffraction peaks 2θ = 9.7, 19.4, 33.3, 38.2, 47.7, 58.7 and 61.9°, respectively of CN-LDH (JCPDS No.14-0191) [32]. The peaks 2θ values of 29.2, 31.3, and 36.8° correspond to the planes (112), (200), and (211), respectively of the tetragonal $CoMn_2O_4$ in MCO-2.5 (JCPDS No.77-0471) [33]. The (400) and (511) planes at 43.7 and 59.1°, respectively are due to the cubic $MnCo_2O_4$ spinel achieved after annealing in air (JCPDS No.23-1237) [33]. From these observations of $Mn_{1+x}Co_{2-x}O_4$, the tetragonal and cubic phases co-exist for $0.3< x<0.9$.

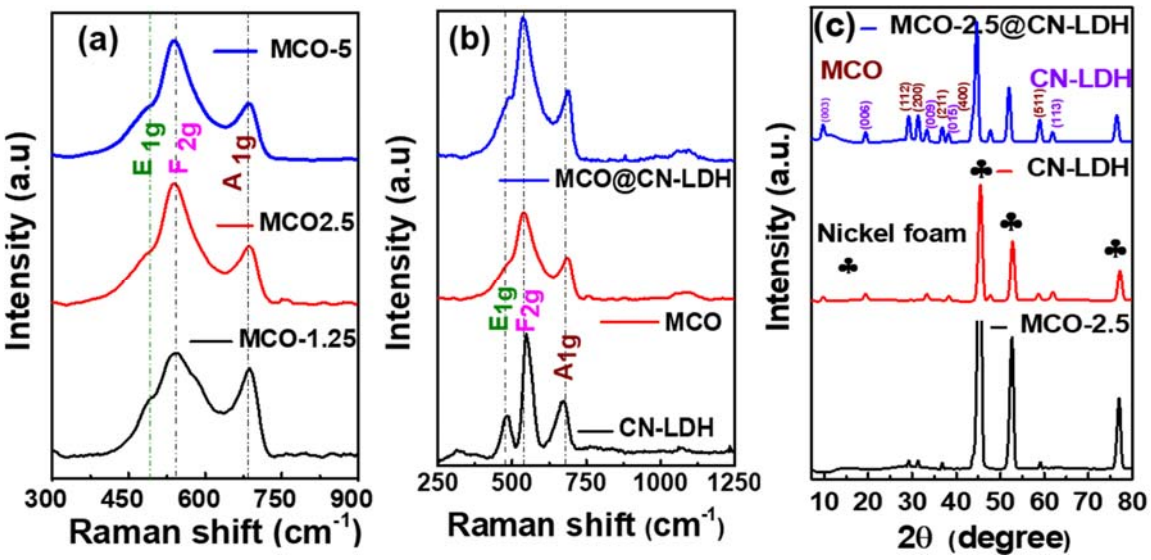

Fig. 3: Raman spectrum of (a) MCO-1.25, MCO-2.5, and MCO-5 and (b) MCO-2.5 CN-LDH, and MCO-2.5@CN-LDH and (c) XRD of MCO-2.5 CN-LDH, and MCO-2.5@CN-LDH.

3.2 Electrochemical performance of the as-synthesized samples

3.2.1 Three-electrode evaluations

Fig. S3(a) displays the GCD of MCO-1.25, MCO-2.5, and MCO-5 at 1 A g^{-1}. The samples show a slanted plateau, reflecting the presence of Faradaic reaction with MCO-2.5 demonstrating longest discharge time. The largest discharge time correspond to the highest specific capacity of MCO-2.5 as illustrated in Fig. S3 (b). Equation (1) was utilised to obtain the specific capacity [34]:

$$Q_S = \frac{1}{3.6} \times I_S \Delta t \quad (1)$$

where, Q_S is the specific capacity (mAh g^{-1}), I_S indicates the specific current (A g^{-1}), and Δt denotes the discharge time (s). The specific capacities for MCO-1.25, MCO-2.5, MCO-5 are 132.9, 238.1 and 97.8 mAh g^{-1}, respectively. Fig. S3 (c) displays the coulombic efficiency

of the samples for 5,000 GCD cycles at 7 A g^{-1}. Equation (2) was used to obtain the columbic efficiency [35]:

$$\eta = \frac{t_D}{t_C} \times 100\ \% \quad (2)$$

where η is the coulombic efficiency (%), t_D and t_C are the times (s) taken to fully discharge and charge, respectively. The coulombic efficiencies are 99.0, 99.7, and 99.8 % for MCO-2.5, CN-LDH, and MCO-2.5@CN-LDH, respectively, which are quasi-perfect which is a characteristic of supercapacitors. The robustness of the electrodeposition synthesis resulted in the superior coulombic efficiency. The general electrochemical comparison shown in Fig. S3 shows a superior performance for MCO-2.5, therefore, all further electrodepositions of CN-LDH on MCO-2.5 were carried-out using a scan rate of 2.5 mV s^{-1} to form composite MCO-2.5@CN-LDH.

Fig. 4(a) shows the GCD traces of MCO-2.5 at 1 A g^{-1} using various electrolytes. 2 M KOH displays the longest discharge time corresponding to the largest specific capacity, and therefore 2 M KOH was selected for further testing of CN-LDH, MCO-2.5@CN-LDH in three electrode configuration and the hybrid supercapacitor device. Fig. 4(b)-(c) displays the electrochemical characterisation of CN-LDH, MCO-2.5, and MCO-2.5@CN-LDH in 3-electrode set-up in 2 M KOH. The mass loading for MCO-2.5 CN-LDH, and MCO-2.5@CN-LDH electrodes were 0.9, 1.1 and 1.2 mg, respectively. Fig. 4(b) displays the CV in a range of 0.0 - 0.4 V vs Ag/AgCl potential at 20 mV s^{-1} with MCO-2.5@CN-LDH exhibiting the highest current response. This can be explained by the improved electrochemical conductivity caused by the CN-LDH and MCO-2.5 complementing each other in the composite. The presence of MCO-2.5 reduces the aggregation of CN-LDH and enhances the ion diffusion. The GCD at 1 A g^{-1} in Fig. 4(c) presents a skewed plateau which further supports the exhibition of the Faradaic nature of the samples in Fig. 4(b). MCO-

2.5@CN-LDH took the longest time to fully discharge, supporting the highest current response seen in Fig. 4(b). The specific capacity as a function of specific current is shown in Fig. 4(d), whereby MCO-2.5@CN-LDH shows the largest specific capacity for all the specific currents recorded (1-10 A g^{-1}).

The rate capabilities at 10 A g^{-1} are 54.3, 58.6 and 87.8 % for MCO-2.5 CN-LDH, and MCO-2.5@CN-LDH, respectively. The high rate capabilities demonstrated by the sample can be attributed to the high electrical conductivity demonstrated by the high current response of the samples and the collaborative effect of both the spinel and the LDH [32,36–41]. Fig. 4(e) displays the Nyquist plot used to evaluate the charge dynamics and the electrical resistivities of the samples. The insert is the enlargement of the plots at the high frequency region to reveal the equivalent series resistance (ESR). The ESR values which corresponds to the high frequency real impedance intercept, as shown in the insert are 1.7, 1.3, 1.6 and 6.4 Ω for MCO-2.5, CN-LDH, MCO-2.5@CN-LDH and NF (nickel-foam), respectively. These ESR values, which are small except for NF, demonstrate that the electrolyte had very small ionic resistance and that the contact resistance between the current collector and the active material (AM) is minimal. The inseparable bonding of the AM and the current collector brought about by the binder-free electrodeposition technique is credited for these small contact resistances. The exclusion of binder in this synthesis approach is very important as the polymeric binder increase the resistance of the electrode materials. The semi-circle in the NF has the largest diameter is evidence of the presence of charge transfer resistance (CTR) which shows the prominence of Faradaic reactions due to the presence of metallic components within the NF. The diameters in MCO-2.5, CN-LDH and MCO-2.5@CN-LDH are significant compared to NF indicating lower CTR. Fig. 4(f) shows the coulombic efficiency and capacity retention of MCO-2.5, CN-LDH, and MCO-2.5@CN-LDH as a function of number of cycles.The coulombic efficiency values are 99.0, 99.7 and 99.8% for

MCO-2.5, CN-LDH, and MCO-2.5@CN-LDH, respectively. The capacity retentions are 71.7, 72.6, and 87.0 %, The high strength of the bond created by the electrodeposition method is credited for the high capacity retention values while the synergertic effect of the the LDH and spinel endow the composite with significantly superior capacity retention.

MCO-2.5 and CN-LDH complement each other in the composite to endow MCO-2.5@CN-LDH with high redox reactivity, high adsorption property and strong chemical stability. MCO-2.5 helps to reduces the the resistivity due to the aggregation of the while CN-LDH provide an abundant active redox active sites and also benefit from its unique layered structure. It is evident from Fig. 4 that the electrochemical performance of MCO-2.5@CN-LDH exceeds those of the from MCO-2.5 and CN-LDH electrodes. This is attributed to the synergistic effect of enhanced ion diffusion due to the Jahn-Teller of MCO-2.5 and the unique layered structure of CN-LDH resulting in the best electrochemical performance of the individual electrodes.

The electrochemical attributes of the composite MCO-2.5@CN-LDH are detailed in Fig. 5. The CV traces shown in Fig. 5(a) reveal sets of reduction and oxidation peaks in a potential range of 0.0 - 0.4 V vs Ag/AgCl for scan rates of 5 - 100 mV s^{-1}. Nevertheless, the prominence of redox crests diminishes with an increase in scan rate. This is due to the drop in the reversibility of the redox process due to the charge diffusion polarisation in the electrode material. Mn and Co undergo oxidation at the same potential, therefore peaks for Mn and Co are not separated [42]. The reversible reactions in equations (3) - (5) are responsible for the redox crest as indicated below:

$$Mn_{2-x}Co_{1+x}O_4 + H_2O + OH^- \leftrightarrow (2-x)\,MnOOH + (1+x)\,CoOOH + e^- \quad (3)$$

$$MnOOH + OH^- \leftrightarrow MnO_2 + H_2O + e^- \quad (4)$$

$$CoOOH + OH^- \leftrightarrow CoO_2 + H_2O + e^- \quad (5)$$

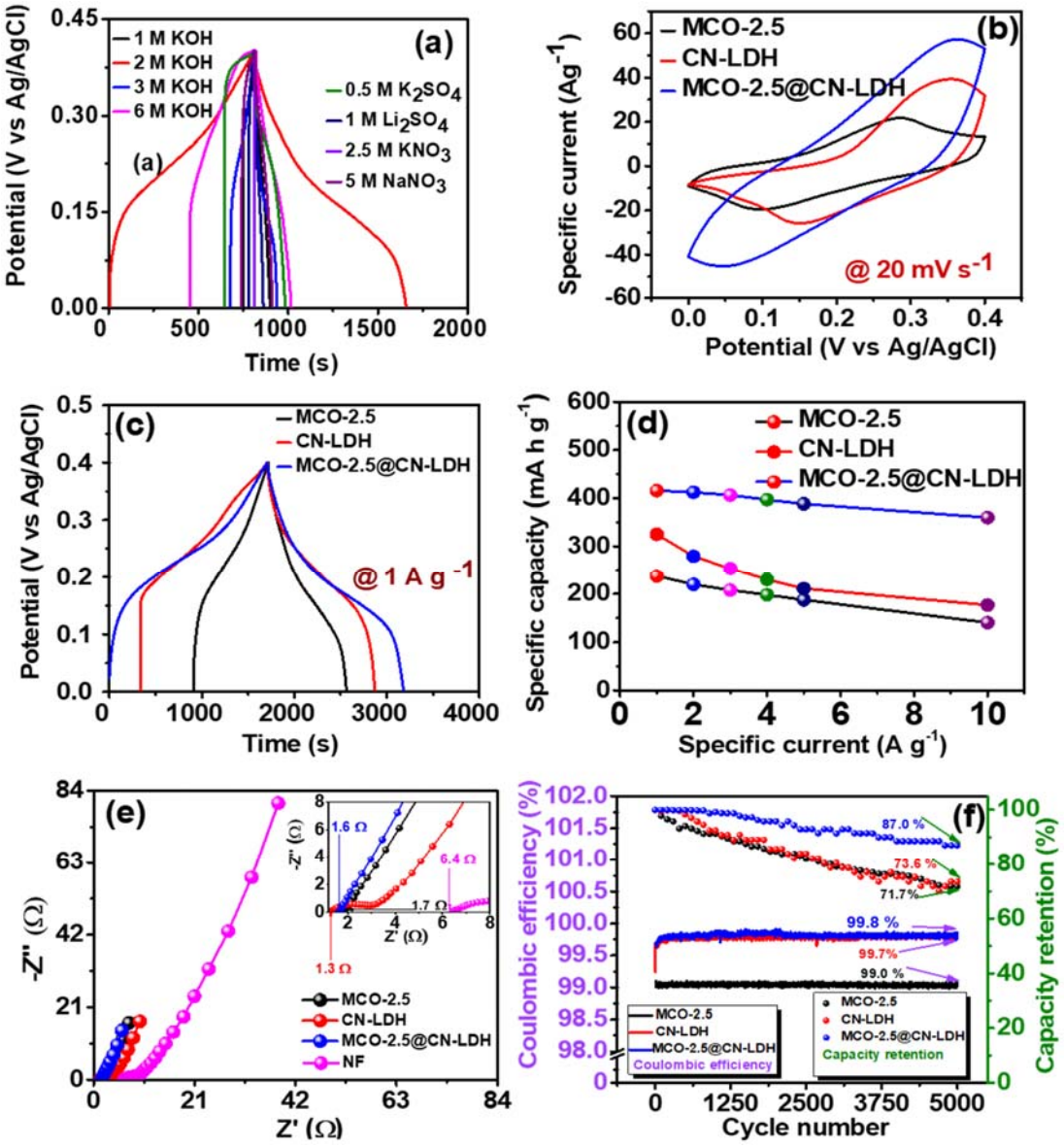

Fig. 4: (a) GCD for MCO-2.5 at 1 A g^{-1} using different electrolytes, Fig (b)- (f) indicated the electrochemical measurements in 2 M KOH electrolyte: (b) the CV traces, (c) GCD traces, (d) specific capacity vs specific current, (e) EIS Nyquist plot with insert, and (f) capacity retention of MCO-2.5, CN-LDH, and MCO-2.5@CN-LDH, respectively.

For a better understanding of the energy storage mechanisms and charge storage contributions, the power laws expressed by equations (6) and (7) were used [43]:

$$I(V) = a\,\nu^{b} \quad (6)$$

$$\log I(V) = a + b\,log\,\nu \quad (7)$$

I (V) is the peak current at a given scan rate ν given in mV s^{-1}, *a* and *b* are constants. For pure surface-controlled processes, *b* equals 1 while for pure diffusion-controlled processes *b* equals 0.5. Fig. 5(b) indicates a plot of log I vs log ν. From the gradient of the linear plot, *b* equals 0.54 and 0.53 for anodic and cathodic processes, respectively. Since the values of b are between 0.5 and 1, both processes have a contribution, however, the diffusion-controlled process dominates.

To evaluate the contribution of diffusion-controlled and capacitive processes, equations (8) and (9) were used:

$$I(V) = K_1\nu + K_2\sqrt{\nu} \quad (8)$$

$$\frac{I(V)}{\sqrt{\nu}} = K_1\sqrt{\nu} + K_2 \quad (9)$$

$K_1\nu\ and\ K_2\sqrt{\nu}$ signify the capacitive and diffusion-controlled processes, respectively. By plotting $\frac{I(V)}{\sqrt{\nu}}\ vs\ \sqrt{\nu}$, the values of the constants, K_1 and K_2 can be obtained from the gradient and the y-intercept, respectively. Fig 5(c) shows the capacitive and diffusion controlled contribution for a range of scan rates from 5 - 100 mV s^{-1}. It is evident that the charge storage mechanism involve both capacitive and diffusion-controlled processes. At a scan rate of 5 mV s^{-1}, the diffusion and capacitive contributions are 70.9 and 29.1 %, respectively while at a high scan rate of 100 mV s^{-1}, the contributions changes to 35.2 and 64.8 %, respectively. This confirms the pseudocapacitive nature of the MCO-2.5@CN-LDH electrode in 2 M

KOH electrolyte. Table S1 compares the capacitive contribution of this work with LDH based electrode materials and composites reported in the literature at 5 mV s^{-1}. The comparison show that the range contribution in this work is within the range of the percentage in the literature.

The GCD of MCO-2.5@CN-LDH is shown in Fig. 5(d) at a specific currents of 1 - 10 A g^{-1}. The pseudocapacitive behaviour of the samples is evident in the lack of a flat plateau at the higher specific currents which is the feature of battery-type storage structure. Fig 5 (e) shows the EIS Nyquist plot of MCO-2.5@CN-LDH whereas the insert shows the equivalent circuit. The equivalent circuit shows the ESR (R_S) which corresponds to the real impedance intercept at the high frequency region with a low value of 1.63 Ω and is comparable to the experimental value of 1.60 Ω. The R_S is in series with a branch containing the constant phase element (CPE) Q, the charge transfer resistance (CTR) denoted by the component (R_{CT}) and the Warburg component (Z_W). R_{CT} proves the presence of Faradaic reactions. The CPE is due to the capacitor behaving non ideally, and Z_W represent the opposition to ion diffusion. The components are in turn in series with the capacitance element (C) corresponding to the slanted line in the low frequency region.

Fig. 5(f) shows the stability results indicating the coulombic efficiency and a capacity retention as a function of number of cycles for MCO-2.5@CN-LDH composite sample. The coulombic efficiency and capacity retention show large values of 99.8 % and 87.0 %, respectively. The synergistic effect of chemical stability of MCO-2.5 and great ion exchange capability of CN-LDH coupled with the robust bonding of the electrode material and current collector brought about by the electrodeposition techniques is credited for this huge stability values after 5,000 GCD cycles. Due to its exceptional electrochemical attributes, MCO-2.5@CN-LDH was selected for incorporation into hybrid device.

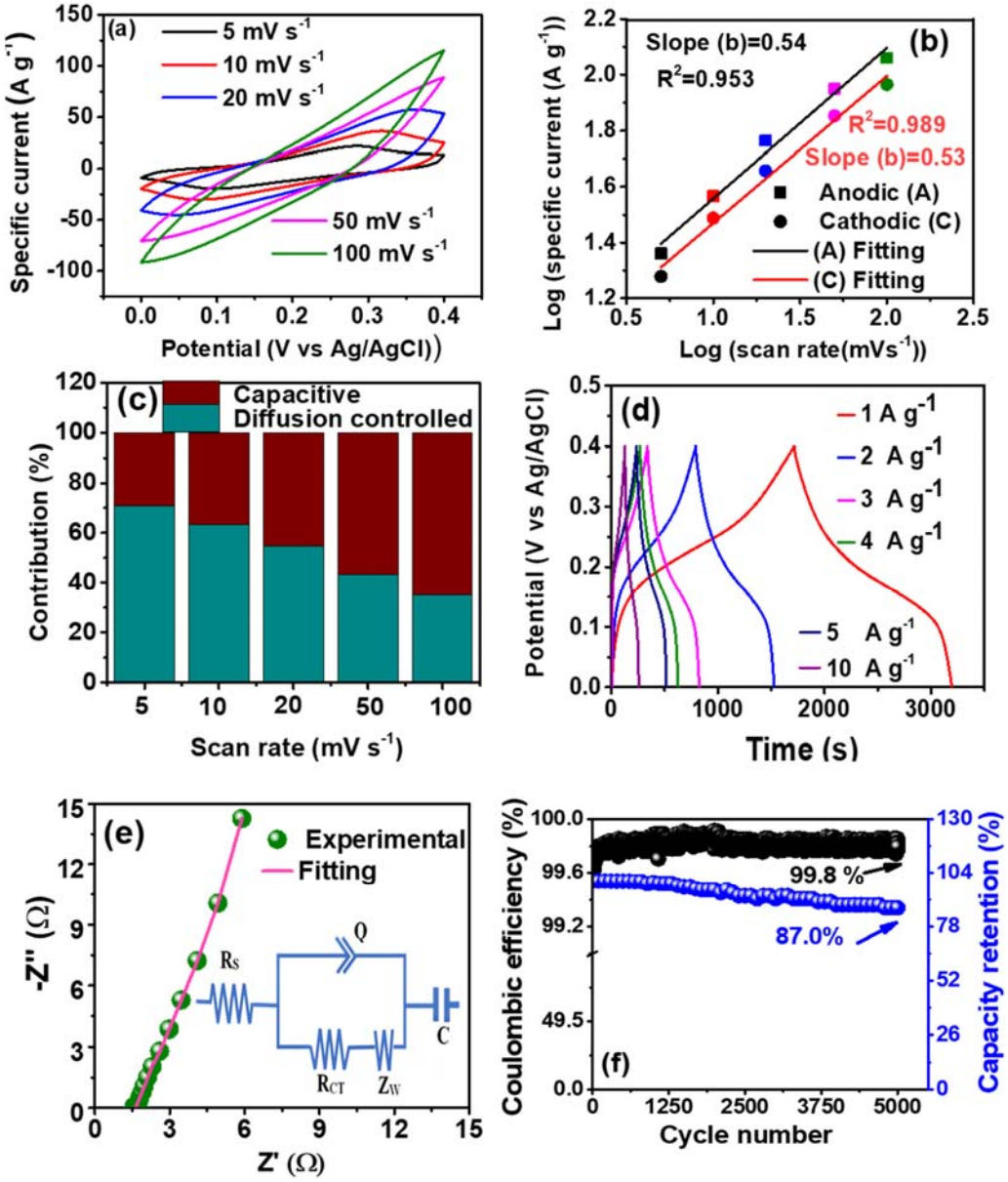

Fig. 5: (a) CV traces, (b) The dependence of log current on log scan rate (power law - anodic and cathodic), (c) Contribution (%) of capacitive and diffusion-controlled charge storage, (d) GCD curves, (e) The Nyquist plot with an inset representing the equivalent circuit, and (f) Coulombic efficiency and capacity retention as a function of cycle number for MCO-2.5@CN-LDH.

Table 1 compares the electrochemical capabilities of MCO composites based electrodes which were reported from the literature. MCO-2.5@CN-LDH (this work) generated the highest specific capacity of 415.9 mAh g^{-1} at 1 A g^{-1}. The table also show high stability results for the synthesis method used in this study which involved the electrodeposition (binder free) and annealing process. It was observed that the electrodeposition synthesis route leads to capacity retentions values which are comparable to other synthesis methods. These highly competitive electrochemical values indicate the coherence of the LDH and spinel in a composite synthesized through electrodeposition and calcination procedures.

Table 1: Electrochemical performance of recently reported manganese cobaltite composites in three-electrode system.

Material	**Synthesis method**	**Capacity (mAh g^{-1})**	**Capacity retention/ (cycles)**	**Ref.**
$Mn_{1.5}Co_{1.5}O_4$	Hydrothermal and calcination	618 (0.4 A g^{-1})	90% (300)	[44]
$MnCo_2O_{4.5}$ /$NiCo_2O_4$	Hydrothermal and calcination	278.4 (1 A g^{-1})	93% (2000)	[45]
$MnCo_2O_{4.5}$ /GCD	Hydrothermal and calcination	225.7 (1 A g^{-1})	80% (2000)	[46]
$MnCo_2O_{4.5}$/RGO	Hydrothermal and calcination	129.7 (1 Ag^{-1})	95% (5000)	[42]
GW-MCO	Microwave	109.3 (20 m V s^{-1})	92.3% (5000)	[47]
MnX_2O_4/GNF	Hydrothermal	237.8 (1 A g^{-1})	80% (3500)	[48]
MCO-2.5@CN-LDH	**Electrodeposition and calcination**	**415.9 (1 A g^{-1})**	**87% (5000)**	**This work**

3.2.2 Electrochemical properties of the hybrid supercapacitor device

A hybrid device MCO-2.5@CN-LDH//CCBW was assembled with the intention to assess the true performance of the MCO-2.5@CN-LDH electrode a full-cell system. CCBW from our previous study was used as the negative electrode [29]. The specific capacitance of the CCBW was measured in three-electrode in 2 M KOH from GCD curves. The GCD of CCBW is shown in the supporting information as Fig S4 (a) in a potential range -0.9 to 0V vs Ag vs AgCl. The specific capacitance range was 30.4-184.4 F g^{-1} as shown in the specific capacitance vs specific current graph in Fig S4 (b).

The analysis was carried-out in 2 M KOH electrolyte in a two-electrode set-up. To avoid a scenario where one electrode will end up charging the other, the charge in each electrode was balanced. To achieve this, the mass ratio of the electrode materials was determined through the mass balance equation (10) [49]:

$$\frac{m_+}{m_-} = \frac{C_{s-} \times V_{S-}}{3.6 Q_{S+}} \tag{10}$$

Here, the negative and positive electrode masses (mg) are denoted as m_- and m_+, the positive electrode specific capacity (mAh g^{-1}) is Q_{S+}, while C_{S-} is the negative electrode's specific capacitance (F g^{-1}), and the negative electrode potential (V) is V_{S-}. For the hybrid device, the mass of the material negative and on each electrodes was 5.4 mg cm^{-2} and 0.6 mg cm^{-2} respecively, corresponding to the mass ratio of m-/m+ was 9:1.

The CV of an individual CCBW negative and MCO-2.5@CN-LDH positive electrodes at 20 mV s^{-1} are indicated in Fig. 6 (a). CCBW indicates a rectangular EDLC trace CV which displays the capacitive behaviour with a performance at -0.9 to 0 V vs Ag/AgCl, whereas MCO-2.5@CN-LDH reveals the Faradaic performance at 0.0-0.4 V vs Ag/AgCl. The CV of the hybrid device at a scan rates of 5 - 100 mV s^{-1} is shown in Fig. 6 (b). The EDLC

features manifest at an approximate cell potential range of 0-0.8 V. In the potential range 0.8-1.6 V, the Faradaic behaviour becomes more predominant. This proves that the contribution of negative and positive electrodes in the device occurs at lower and high cell potentials, respectively. However, the disappearance of the redox peaks as the scan rate increases confirms the change from Faradaic to pseudocapacitive nature of the composite material which is credited to the incorporation of the EDLC material within the device. Fig. 6(c) presents the GCD at a specific current from 1 to 10 A g^{-1}. The symmetry in the curves shows the reversibility of the redox reactions. There are no clear horizontal plateaux in the GCD curves showing that the charge storage mechanism is not entirely EDLC or purely Faradaic but rather pseudocapacitive. Fig. 6 (d) indicates the variation of specific capacity with specific current from 1-10 A g^{-1}. The greatest specific capacity of 59.0 mAh g^{-1} occurs at 1 A g^{-1} corresponding to a rate capability of 52 % at 10 A g^{-1}. Fig. 6(e) relates the stability measurements of the device. After 10,000 GCD cycles at 7 A g^{-1}, the device was able to preserve a coulombic efficiency of 99.8 % and a capacity retention of 81.6 %. The lack of binders in MCO-2.5@CN-LDH was responsible for such high stability [50]. To obtain the specific energy (E_s) and specific power (P_s), equations (11) and (12) were used [51], [52]:

$$E_s\ (Wh\ kg^{-1}) = \frac{I_s}{3.6} \int V(t)dt \tag{11}$$

$$P_s\ (W\ kg^{-1}) = 3600 \times \frac{Es}{\Delta t} \tag{12}$$

where $\int V(t)dt$ denotes the integral (Vs) representing the area under the discharge GCD curve, I_s is the specific current (A g^{-1}) of the GCD curve, and Δt represents the discharge time (s).

This MCO-2.5@CN-LDH//CCBW hybrid device delivered a great specific energy of 55.8 Wh kg^{-1} at 1 A g^{-1} with corresponding specific power of 940 W kg^{-1}. For a comparison of the energy storage and power delivery of this device with those of manganese cobaltite based

materials reported in the literature, the Ragone plot in Fig. 6(f) was used for representation. From the plot it is clear that the MCO-2.5@CN-LDH//CCBW hybrid device outperforms some of the similar devices in the literature in terms of energy storage and rate of energy delivery [20,42,45,46,48,53].

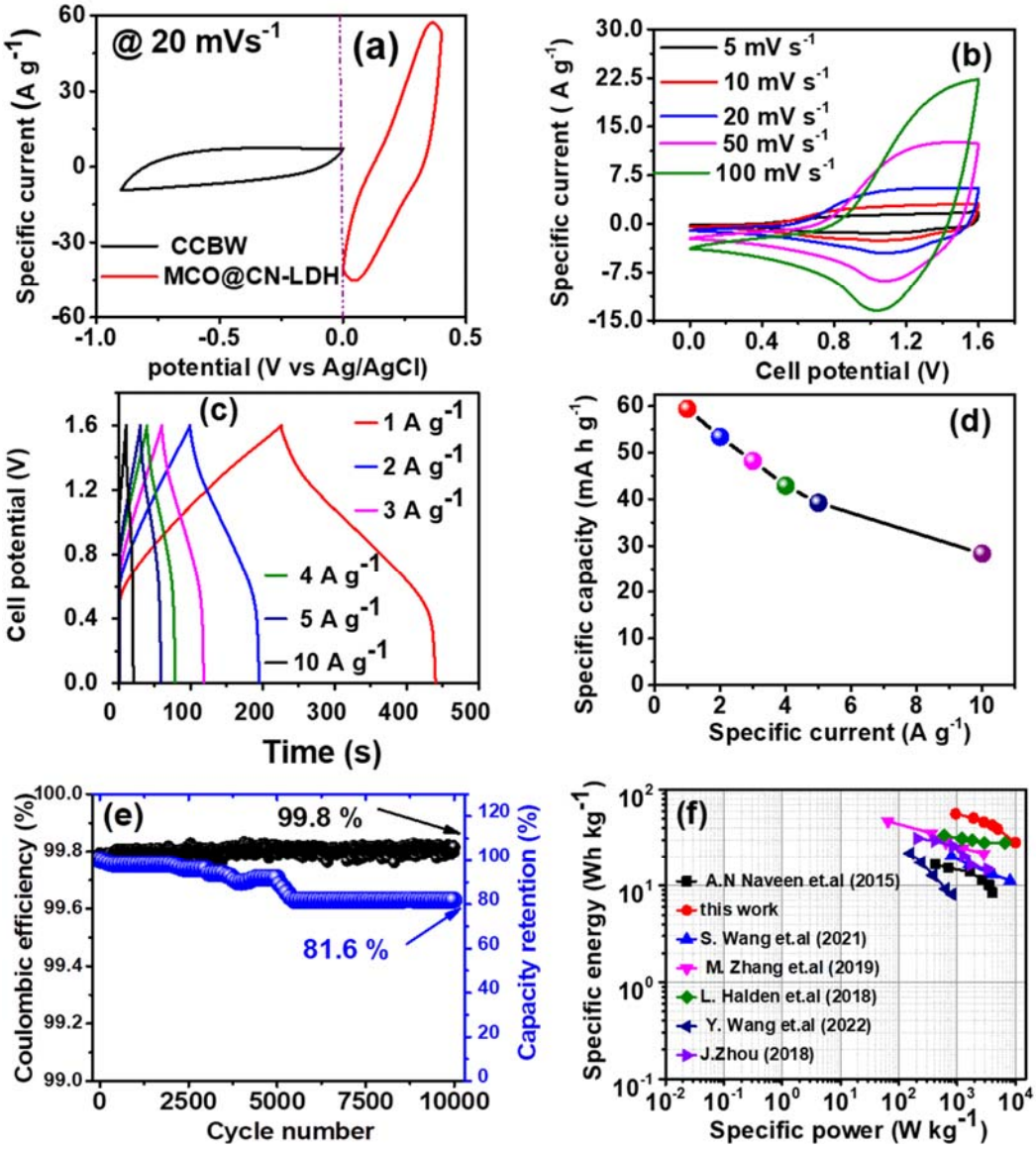

Fig. 6 (a): CV traces of the negative and positive electrodes at 20 mV s^{-1}, Fig (b)-(e) show the electrochemical performance of the MCO-2.5@CN-LDH//CCBW device. (b) CV traces at various scan rates, (c) GCD traces at a range of specific currents, (d) the specific capacity vs specific current, (e) coulombic efficiency and capacity retention vs cycle number and (f)

Ragone plot of MCO-2.5@CN-LDH//CCBW hybrid device compared to other similar devices in the literature.

The maximum power (P_{MAX}) is delivered when the ESR matches the load resistance, in which the P_{MAX} in this study was calculated from equation 13 below [54] :

$$P_{MAX}\ (kW\ kg^{-1}) = \frac{V^2}{4m \times R_S} \qquad (13)$$

where m is the total mass (g) of the AM in the hybrid device, V is the cell potential (V), and R_S (**Ω**) is ESR of the assembled device. The value of P_{MAX} for the device was found to be 106.7 kW kg. $^{-1}$.

This phenomenal electrochemical performance of the hybrid device can be credited to the Faradaic and EDLC charge storage in the positive and negative electrodes complementing each other. The high electrical conductivity and wide operating potential of CCBW leads the high specific power and cyclic stability while the large specific capacity of MCO-2.5@CN-LDH is responsible for the huge specific energy. The electrochemical properties of earlier reported hybrid devices which incorporate manganese cobaltite are displayed in Table 2 for a particular lowest specific current. The MCO-2.5@CN-LDH//CCBW hybrid device yielded a substantial specific energy of 55.8 Wh kg^{-1} corresponding to a specific power of 940 W kg^{-1}.

Table 2: Comparison of manganese cobaltite-based hybrid devices reported in the literature in terms of electrochemical performance.

Device	Electrolyte	Cell potential (V)	E_S (Wh kg^{-1})	P_S (W kg^{-1})	Ref.
$MnCo_2O_4$@NiCo-LDH/NF//AC	6 M KOH	1.6	21.3	160	[20]
(MCO/Ni)-15 min//PAC/Ni	(CMC)-$LiNO_3$ gel	2.0	27.6	1010	[33]
$MnCo_2O_{4.5}$/GCD//RGO	1 M KOH	1.3	46	66	[46]
$MnCo_2O_{4.5}$-$NiCo_2O_4$ //Fe-rGO	2 M KOH	1.2	34	597	[45]
$MnCo_2O_4$@Co_3O_4//AC	2 M KOH	1.5	31	208.5	[53]
$MnCo_2O_4$//rGO	1 M KOH	1.6	53.7	1600	[55]
MCO-2.5@CN-LDH//CCBW	**2 M KOH**	**1.6**	**55.8**	**940**	**This work**

The Nyquist plot in Fig. 7(a) shows the synthesized device's experimental results alongside the fitting line. The equivalent circuit used to fit is shown in the inset. The small ESR value (R_S) of 1.87 Ω signified the diminished contact resistance between the AM and the current collector. The circuit displays a small R_{CT} of 3.47 Ω. The lowered semicircle is due to the presence of the CPE. The CPE therefore makes R_{CT} appear smaller than its actual value. The resistance due to the leakage currents, R_L is in series with the EDLC capacitance. R_L has a value of 1.73 Ω, and it leads to the curve deflecting further from the imaginary impedance axes decreasing the size of the phase angle from -90^o. The Z_w which is parallel to R_L and C further diverges the slope in the low frequency zone. The EIS Nyquist plots before and after cycling is shown in Fig. 7(b). The reduction of the resistance at the boundary between the electrolyte and the electrode and between AM-current collector cause the R_S to drop to 0.980 Ω after 10,000 GCD cycles. Nevertheless, the gradient of the trace after 10,000 cycles shows an increase in the diffusion length on the electrolyte-electrode interface caused by the decomposition of the water molecules in the electrolyte [56]. Fig. 7(c) is indicating the Bode

plot with the phase angle as a function of frequency. The phase angle at the low frequency region is -67^{o} which is not very close to -90^{o} signifying the occurrence of both capacitive and Faradaic characteristics in the device. The variance of real capacitance $C'(\omega)$) and imaginary capacitance ($C''(\omega)$ with frequency (f) is demonstrated in Fig. 7(d). These capacitances are calculated from the equations expressed below [26]:

$$Z'(\omega) = \omega C''(\omega)|Z(\omega)| \tag{14}$$

$$Z^{''}(\omega) = \omega C^{'}(\omega)|Z(\omega)| \tag{15}$$

where, $|Z(\omega)|, Z'(\omega)$ and $Z''(\omega)$ are the magnitude of impedance, real and imaginary impedances (**Ω**), respectively. ω denote the angular frequency (rad s^{-1}) which is given by $\omega = 2\pi f$. The capacitance (F) of the device which can be accessible and transferred is denoted by C′(ω*)* and it corresponds to a maximum value of 0.44 F at low frequency as shown in Fig. 7(d). C′′(ω) depicts the electrode's energy drop caused by non-reversible reactions. The C′′(ω) has a crest of 0.24 F at 0.031 Hz. The time τ taken to fully charge the device is 4.5s obtained from the plot using 2πfτ = 1. This small value shows that the charging is very fast for this device.

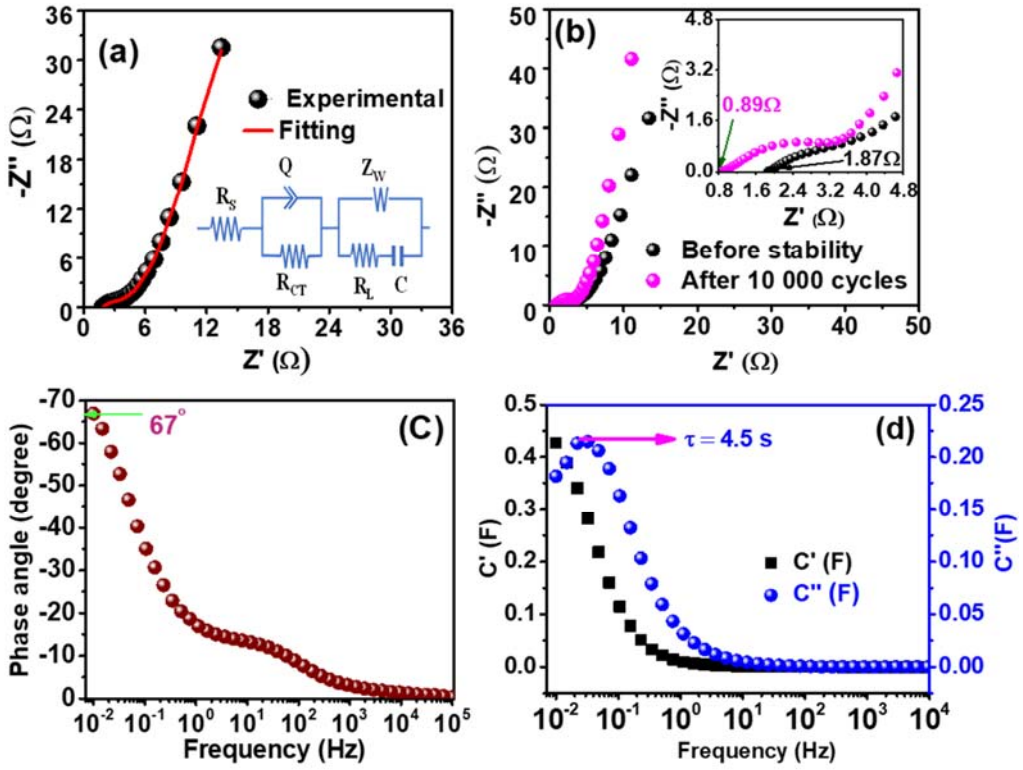

Fig. 7: (a) Nyquist plot of the experimental data with the fitting curve using an equivalent circuit as the inset to the figure, (b) Nyquist plot before and after cycling stability with inset which is magnification in the high frequency region, (c) Bode plot and (d) imaginary and real capacitance vs frequency of the hybrid device.

4.0 Conclusion

A dual electrodeposition approach and calcination was employed to synthesize MCO-2.5, CN-LDH, and MCO-2.5@CN-LDH samples. The best electrochemical performance was achieved in the composite electrode material (MCO-2.5@CN-LDH). It yielded the highest specific capacity of 415.9 mAh g^{-1} at specific current of 1 A g^{-1}. After 5,000 GCD cycles performed at 7 A g^{-1}, the electrode produced a coulombic efficiency of 99.8 %. The electrode was used to assemble a hybrid device fabricated with activated with CCBW as the negative electrode. This MCO-2.5@CN-LDH//CCBW hybrid device produced a great specific

energy of 55.8 Wh kg^{-1} at 1 A g^{-1} corresponding to a specific power of 940.4 W kg^{-1}. Stability tests of the device for 10,000 at a specific current of 7 A g^{-1} yielded a coulombic efficiency of 99.8 % and a capacity retention of 81.6 %. Due to these satisfactory performances, the hybrid device is a potential candidate for inclusion in high energy performaning devices.

Acknowledgements

This research was facilitated by the South African Research Chairs Initiative (SARChI) of the Department of Science and technology and the National Research foundation (NRF) South Africa (Grant number. 61056). All the ideas, findings, recommendations, and conclusions in this work are from of author(s) therefore NRF does not take any liability in this regard. Gift Rutavi recognises the support from NRF through SARChI in Carbon materials.

References

[1] R. Vakulchuk, I. Overland, D. Scholten, Renewable energy and geopolitics: A review, Renew. Sustain. Energy Rev. 122 (2020) 109547. https://doi.org/10.1016/j.rser.2019.109547.

[2] S. Ganesan, U. Subramaniam, A.A. Ghodke, R.M. Elavarasan, K. Raju, M.S. Bhaskar, Investigation on sizing of voltage source for a battery energy storage system in microgrid with renewable energy sources, IEEE Access. 8 (2020) 188861–188874. https://doi.org/10.1109/ACCESS.2020.3030729.

[3] M. Shafiul Alam, F.S. Al-Ismail, A. Salem, M.A. Abido, High-level penetration of renewable energy sources into grid utility: Challenges and solutions, IEEE Access. 8 (2020) 190277–190299. https://doi.org/10.1109/ACCESS.2020.3031481.

[4] Y. Li, W. Lin, L. Xue, J. Xie, B. Wei, G. Chen, D. Chen, Facile preparation of V2O3/black fungus-derived carbon composite with hierarchical porosity as a promising electrode for lithium/sodium ion batteries, J. Alloys Compd. 905 (2022) 164258. https://doi.org/10.1016/j.jallcom.2022.164258.

[5] C. Xiong, M. Li, S. Nie, W. Dang, W. Zhao, L. Dai, Y. Ni, Non-carbonized porous lignin-free wood as an effective scaffold to fabricate lignin-free Wood@Polyaniline supercapacitor material for renewable energy storage application, J. Power Sources. 471 (2020) 228448. https://doi.org/10.1016/j.jpowsour.2020.228448.

[6] A. Khan, R.A. Senthil, J. Pan, S. Osman, Y. Sun, X. Shu, A new biomass derived rod-like porous carbon from tea-waste as inexpensive and sustainable energy material for advanced supercapacitor application, Electrochim. Acta. 335 (2020) 135588. https://doi.org/10.1016/j.electacta.2019.135588.

[7] Z. Yang, W. Xu, M. Zhao, W. Yang, J. Xia, Z. Zhou, J. Song, L. Sheng, B. Wei, Ethanol and KOH co-pretreatment towards ultra-high specific surface area carbons for high-rate and high-energy supercapacitors, Chem. Commun. 56 (2020) 15561–15564. https://doi.org/10.1039/d0cc06187e.

[8] J. Dong, S. Li, Y. Ding, Anchoring nickel-cobalt sulfide nanoparticles on carbon aerogel derived from waste watermelon rind for high-performance asymmetric supercapacitors, J. Alloys Compd. 845 (2020) 155701. https://doi.org/10.1016/j.jallcom.2020.155701.

[9] F. Yu, C. Zhang, F. Wang, Y. Gu, P. Zhang, E.R. Waclawik, A. Du, K. Ostrikov, H. Wang, A zinc bromine “supercapattery” system combining triple functions of capacitive, pseudocapacitive and battery-type charge storage, Mater. Horizons. 7 (2020) 495–503. https://doi.org/10.1039/c9mh01353a.

[10] S.J. Patil, N.R. Chodankar, Y.K. Han, D.W. Lee, Carbon alternative

pseudocapacitive V2O5 nanobricks and δ-MnO2 nanoflakes @ α-MnO2 nanowires hetero-phase for high-energy pseudocapacitor, J. Power Sources. 453 (2020) 227766. https://doi.org/10.1016/j.jpowsour.2020.227766.

[11] S. Suriyakumar, P. Bhardwaj, A.N. Grace, A.M. Stephan, Role of Polymers in Enhancing the Performance of Electrochemical Supercapacitors: A Review, Batter. Supercaps. 4 (2021) 571–584. https://doi.org/10.1002/batt.202000272.

[12] D. Han, Y. Zhao, Y. Shen, Y. Wei, L. Mao, G. Zeng, Co3O4 nanowire@ultrathin Ni-Co layered double hydroxide core-shell arrays with vertical transfer channel for high-performance supercapacitor, J. Electroanal. Chem. 859 (2020). https://doi.org/10.1016/j.jelechem.2020.113887.

[13] Y. Li, L. Wang, Y. Qu, B. Wang, J. Yu, D. Song, C. Duan, Y. Yang, Unique 3D bilayer nanostructure basic cobalt carbonate@NiCo–layered double hydroxide nanosheets on carbon cloth for supercapacitor electrode material, Ionics (Kiel). 26 (2020) 1397–1406. https://doi.org/10.1007/s11581-019-03310-z.

[14] G. Zhou, X. Gao, S. Wen, X. Wu, L. Zhang, T. Wang, P. Zhao, J. Yin, W. Zhu, Magnesium-regulated oxygen vacancies of cobalt-nickel layered double hydroxide nanosheets for ultrahigh performance asymmetric supercapacitors, J. Colloid Interface Sci. 612 (2022) 772–781. https://doi.org/10.1016/j.jcis.2021.12.087.

[15] L. Xie, S. Chen, Y. Hu, Y. Lan, X. Li, Q. Deng, J. Wang, Z. Zeng, S. Deng, Construction of phosphatized cobalt nickel-LDH nanosheet arrays as binder-free electrode for high-performance battery-like supercapacitor device, J. Alloys Compd. 858 (2021) 157652. https://doi.org/10.1016/j.jallcom.2020.157652.

[16] J.J. Zhou, Q. Li, C. Chen, Y.L. Li, K. Tao, L. Han, Co3O4@CoNi-LDH core/shell nanosheet arrays for high-performance battery-type supercapacitors, Chem. Eng. J. 350 (2018) 551–558. https://doi.org/10.1016/j.cej.2018.06.023.

[17] S. Megala, M. Sathish, S. Harish, M. Navaneethan, S. Sohila, B. Liang, R. Ramesh, Enhancement of photocatalytic H2 evolution from water splitting by construction of two dimensional gC3N4/NiAl layered double hydroxides, Appl. Surf. Sci. 509 (2020) 144656. https://doi.org/10.1016/j.apsusc.2019.144656.

[18] N.L.W. Septiani, Y.V. Kaneti, Y. Guo, B. Yuliarto, X. Jiang, Y. Ide, N. Nugraha, H.K. Dipojono, A. Yu, Y. Sugahara, D. Golberg, Y. Yamauchi, Holey Assembly of Two-Dimensional Iron-Doped Nickel-Cobalt Layered Double Hydroxide Nanosheets for Energy Conversion Application, ChemSusChem. 13 (2020) 1645–1655. https://doi.org/10.1002/cssc.201901364.

[19] P.F. Wang, T. Jin, J. Zhang, Q.C. Wang, X. Ji, C. Cui, N. Piao, S. Liu, J. Xu, X.Q. Yang, C. Wang, Elucidation of the Jahn-Teller effect in a pair of sodium isomer, Nano Energy. 77 (2020) 105167. https://doi.org/10.1016/j.nanoen.2020.105167.

[20] Y. Wang, Z. Wang, X. Zheng, X. Teng, L. Xu, Y. Yuan, X. Liu, A. Fu, Y. Li, H. Li, Core-sheath heterostructure of MnCo2O4 nanowires wrapped by NiCo-layered double hydroxide as cathode material for high-performance quasi-solid-state asymmetric supercapacitors, J. Alloys Compd. 904 (2022) 164047. https://doi.org/10.1016/j.jallcom.2022.164047.

[21] S. Wang, Y. Zou, F. Xu, C. Xiang, H. Peng, J. Zhang, L. Sun, Morphological control and electrochemical performance of NiCo2O4@NiCo layered double hydroxide as an electrode for supercapacitors, J. Energy Storage. 41 (2021) 102862. https://doi.org/10.1016/j.est.2021.102862.

[22] K. Ramachandran, C. Jeganathan, S. Karuppuchamy, Electrodeposition of nanostructured bilayer CuI@CuSCN as hole transport material for highly efficient inverted perovskite solar cells, J. Alloys Compd. 881 (2021) 160530. https://doi.org/10.1016/j.jallcom.2021.160530.

[23] X. Li, X. Qian, Y. Xu, F. Duan, Q. Yu, J. Wang, L. Chen, Y. Dan, X. Cheng, Electrodeposited cobalt phosphides with hierarchical nanostructure on biomass carbon for bifunctional water splitting in alkaline solution, J. Alloys Compd. 829 (2020) 154535. https://doi.org/10.1016/j.jallcom.2020.154535.

[24] H. Fan, Y. Ma, W. Chen, Y. Tang, L. Li, J. Wang, Facile one-step electrodeposition of two-dimensional nickel-iron bimetallic sulfides for efficient electrocatalytic oxygen evolution, J. Alloys Compd. 894 (2022) 162533. https://doi.org/10.1016/j.jallcom.2021.162533.

[25] H. Wu, P. Liu, M. Yin, Z. Hou, L. Hu, J. Dang, Surface modification engineering on three-dimensional self-supported NiCoP to construct NiCoOx/NiCoP for highly efficient alkaline hydrogen evolution reaction, J. Alloys Compd. 835 (2020) 155364. https://doi.org/10.1016/j.jallcom.2020.155364.

[26] G. Rutavi, D.J. Tarimo, V.M. Maphiri, N. Manyala, Two-step electrodeposition of Hausmannite sulphur reduced graphene oxide and cobalt-nickel layered double hydroxide heterostructure for high-performance supercapacitor, (2022). https://doi.org/10.1002/er.7922.

[27] H. Insight, E.S. Zhitova, H.C. Greenwell, M.G. Krzhizhanovskaya, D.C. Apperley, I. V Pekov, V.N. Yakovenchuk, Thermal Evolution of Natural Layered Double and Cl-Members of the Hydrotalcite Supergroup, (n.d.).

[28] G. Rutavi, D.J. Tarimo, V.M. Maphiri, N. Manyala, Two-step electrodeposition of Hausmannite sulphur reduced graphene oxide and cobalt-nickel layered double hydroxide heterostructure for high-performance supercapacitor, Int. J. Energy Res. (2022) 1–14. https://doi.org/10.1002/er.7922.

[29] D.J. Tarimo, K.O. Oyedotun, N.F. Sylla, A.A. Mirghni, N.M. Ndiaye, N. Manyala, Waste chicken bone-derived porous carbon materials as high performance electrode

for supercapacitor applications, J. Energy Storage. 51 (2022) 104378. https://doi.org/10.1016/j.est.2022.104378.

[30] R. Hassandoost, A. Kotb, Z. Movafagh, M. Esmat, R. Guegan, S. Endo, W. Jevasuwan, N. Fukata, Y. Sugahara, A. Khataee, Y. Yamauchi, Y. Ide, E. Doustkhah, Nanoarchitecturing bimetallic manganese cobaltite spinels for sonocatalytic degradation of oxytetracycline, Chem. Eng. J. 431 (2022). https://doi.org/10.1016/j.cej.2021.133851.

[31] Y. Zhu, S. An, X. Sun, D. Lan, J. Cui, Y. Zhang, W. He, Core-branched NiCo2S4@CoNi-LDH heterostructure as advanced electrode with superior energy storage performance, Chem. Eng. J. 383 (2020) 123206. https://doi.org/10.1016/j.cej.2019.123206.

[32] N. Zhao, H. Fan, M. Zhang, C. Wang, X. Ren, H. Peng, H. Li, X. Jiang, X. Cao, Preparation of partially-cladding NiCo-LDH/Mn3O4 composite by electrodeposition route and its excellent supercapacitor performance, J. Alloys Compd. 796 (2019) 111–119. https://doi.org/10.1016/j.jallcom.2019.05.023.

[33] G.T. Pan, S. Chong, T.C.K. Yang, C.M. Huang, Electrodeposited porous mn1.5co1.5o4/ni composite electrodes for high-voltage asymmetric supercapacitors, Materials (Basel). 10 (2017) 1–12. https://doi.org/10.3390/ma10040370.

[34] V.N. Kitenge, K.O. Oyedotun, O. Fasakin, D.J. Tarimo, N.F. Sylla, X. Van Heerden, N. Manyala, Enhancing the electrochemical properties of a nickel–cobalt-manganese ternary hydroxide electrode using graphene foam for supercapacitors applications, Mater. Renew. Sustain. Energy. 10 (2021) 1–16. https://doi.org/10.1007/s40243-021-00192-y.

[35] D.T. Bakhoum, K.O. Oyedotun, S. Sarr, N.F. Sylla, V.M. Maphiri, N.M. Ndiaye, B.D. Ngom, N. Manyala, A study of porous carbon structures derived from

composite of cross-linked polymers and reduced graphene oxide for supercapacitor applications, J. Energy Storage. 51 (2022) 104476. https://doi.org/10.1016/j.est.2022.104476.

[36] Y. Wang, C. Shen, L. Niu, Z. Sun, F. Ruan, M. Xu, S. Shan, C. Li, X. Liu, Y. Gong, High rate capability of mesoporous NiWO4–CoWO4 nanocomposite as a positive material for hybrid supercapacitor, Mater. Chem. Phys. 182 (2016) 394–401. https://doi.org/10.1016/j.matchemphys.2016.07.047.

[37] L. Zhang, G. Shi, Preparation of highly conductive graphene hydrogels for fabricating supercapacitors with high rate capability, J. Phys. Chem. C. 115 (2011) 17206–17212. https://doi.org/10.1021/jp204036a.

[38] J. Acharya, M. Park, T.H. Ko, B.S. Kim, Leaf-like integrated hierarchical NiCo2O4 nanorods@Ni-Co-LDH nanosheets electrodes for high-rate asymmetric supercapacitors, J. Alloys Compd. 884 (2021). https://doi.org/10.1016/j.jallcom.2021.161165.

[39] J. Acharya, T.H. Ko, M.K. Seo, M.S. Khil, H.Y. Kim, B.S. Kim, Engineering the Hierarchical Heterostructures of Zn-Ni-Co Nanoneedles Arrays@Co-Ni-LDH Nanosheets Core-Sheath Electrodes for a Hybrid Asymmetric Supercapacitor with High Energy Density and Excellent Cyclic Stability, ACS Appl. Energy Mater. 3 (2020) 7383–7396. https://doi.org/10.1021/acsaem.0c00781.

[40] Y. Ji, F. Chen, S. Tan, F. Ren, Hierarchical coral-like MnCo2O4.5@Co-Ni LDH composites on Ni foam as promising electrodes for high-performance supercapacitor, Nanotechnology. 33 (2022). https://doi.org/10.1088/1361-6528/ac3a3c.

[41] S. Jo, N. Jayababu, D. Kim, Rational design of cobalt-iron bimetal layered hydroxide on conductive fabric as a flexible battery-type electrode for enhancing the

performance of hybrid supercapacitor, J. Alloys Compd. 904 (2022) 164082. https://doi.org/10.1016/j.jallcom.2022.164082.

[42] A.N. Naveen, S. Selladurai, A 1-D/2-D hybrid nanostructured manganese cobaltite-graphene nanocomposite for electrochemical energy storage, RSC Adv. 5 (2015) 65139–65152. https://doi.org/10.1039/c5ra09288d.

[43] A. Elgendy, N.M. El Basiony, F. El-Taib Heakal, A.E. Elkholy, Mesoporous Ni-Zn-Fe layered double hydroxide as an efficient binder-free electrode active material for high-performance supercapacitors, J. Power Sources. 466 (2020) 228294. https://doi.org/10.1016/j.jpowsour.2020.228294.

[44] J. Li, S. Xiong, X. Li, Y. Qian, Spinel Mn 1.5Co 1.5O 4 core-shell microspheres as Li-ion battery anode materials with a long cycle life and high capacity, J. Mater. Chem. 22 (2012) 23254–23259. https://doi.org/10.1039/c2jm35607d.

[45] L. Halder, A. Maitra, A.K. Das, R. Bera, S.K. Karan, S. Paria, A. Bera, S.K. Si, B.B. Khatua, High performance advanced asymmetric supercapacitor based on ultrathin and mesoporous MnCo2O4.5-NiCo2O4 hybrid and iron oxide decorated reduced graphene oxide electrode materials, Electrochim. Acta. 283 (2018) 438–447. https://doi.org/10.1016/j.electacta.2018.06.184.

[46] M. Zhang, W. Liu, R. Liang, R. Tjandra, A. Yu, Graphene quantum dot induced tunable growth of nanostructured MnCo2O4.5 composites for high-performance supercapacitors, Sustain. Energy Fuels. 3 (2019) 2499–2508. https://doi.org/10.1039/c9se00341j.

[47] R. Kumar, M.M. Abdel-Galeil, K.Z. Ya, K. Fujita, W.K. Tan, A. Matsuda, Facile and fast microwave-assisted formation of reduced graphene oxide-wrapped manganese cobaltite ternary hybrids as improved supercapacitor electrode material, Appl. Surf. Sci. 481 (2019) 296–306. https://doi.org/10.1016/j.apsusc.2019.03.085.

[48] S. Wang, Y. Xu, J. Qin, S. Chen, Y. Du, Y. Xu, J. Xu, W. Zhou, One-pot synthesis of MnX2O4(X = Co, Ni)/graphite nanoflakes composites as high-performance supercapacitor electrodes, Mater. Res. Bull. 141 (2021). https://doi.org/10.1016/j.materresbull.2021.111349.

[49] B.A. Mahmoud, A.A. Mirghni, K.O. Oyedotun, O. Fasakin, N. Manyala, Nanoplatelets ammonium nickel-cobalt phosphate graphene foam composite as novel electrode material for hybrid supercapacitors, J. Alloys Compd. 883 (2021) 160897. https://doi.org/10.1016/j.jallcom.2021.160897.

[50] C. Sun, X. Li, Z. Cai, F. Ge, Carbonized cotton fabric in-situ electrodeposition polypyrrole as high-performance flexible electrode for wearable supercapacitor, Electrochim. Acta. 296 (2019) 617–626. https://doi.org/10.1016/j.electacta.2018.11.045.

[51] D.J. Tarimo, K.O. Oyedotun, A.A. Mirghni, B. Mutuma, N.F. Sylla, P. Murovhi, N. Manyala, Enhanced electrochemical performance of supercapattery derived from sulphur-reduced graphene oxide/cobalt oxide composite and activated carbon from peanut shells, Int. J. Hydrogen Energy. 45 (2020) 33059–33075. https://doi.org/10.1016/j.ijhydene.2020.09.142.

[52] A.A. Mirghni, K.O. Oyedotun, O. Fasakin, B.A. Mahmoud, D.J. Tarimo, N. Manyala, High-performance bimetallic Ni-Mn phosphate hybridized with 3-D graphene foam for novel hybrid supercapacitors, J. Energy Storage. 31 (2020) 101584. https://doi.org/10.1016/j.est.2020.101584.

[53] J.J. Zhou, X. Han, K. Tao, Q. Li, Y.L. Li, C. Chen, L. Han, Shish-kebab type MnCo2O4@Co3O4 nanoneedle arrays derived from MnCo-LDH@ZIF-67 for high-performance supercapacitors and efficient oxygen evolution reaction, Chem. Eng. J. 354 (2018) 875–884. https://doi.org/10.1016/j.cej.2018.08.102.

[54] M.Z. Iqbal, M.M. Faisal, S.R. Ali, Integration of supercapacitors and batteries towards high-performance hybrid energy storage devices, Int. J. Energy Res. 45 (2021) 1449–1479. https://doi.org/10.1002/er.5954.

[55] J. Xu, Y. Sun, M. Lu, L. Wang, J. Zhang, E. Tao, J. Qian, X. Liu, Fabrication of the porous MnCo2O4 nanorod arrays on Ni foam as an advanced electrode for asymmetric supercapacitors, Acta Mater. 152 (2018) 162–174. https://doi.org/10.1016/j.actamat.2018.04.025.

[56] H. Liang, T. Lin, S. Wang, H. Jia, C. Li, J. Cao, J. Feng, W. Fei, J. Qi, A free-standing manganese cobalt sulfide@cobalt nickel layered double hydroxide core-shell heterostructure for an asymmetric supercapacitor, Dalt. Trans. 49 (2019) 196–202. https://doi.org/10.1039/c9dt03974k.